Green Chemistry

ROYAL SOCIETY OF CHEMISTRY

PAPER

View Article Online
View Journal | View Issue

**Cite this:** *Green Chem.*, 2025, **27**, 9144

# Triazine-cored donor–acceptor covalent organic framework promotes highly efficient photocatalytic synthesis of $H_2O_2$†

Lihua Li, *‡[a] Xin Yao,‡[a] Weizhi Ou,[a] Jing Chai,[a] Ru Ma,[a] Chenglong Ran,[a] Anzhi Ma,[a] Xiaojun Shi,[a] Pifeng Wei,[b] Hong Dong, [c] Hongpeng Zhou,*[d] Wenbing Yang,[e] Hai-Chao Hu,[e] Jian-Feng Wu,[e] Hui Peng [a] and Guofu Ma *[a]

Received 9th April 2025,
Accepted 16th June 2025

DOI: 10.1039/d5gc01754h

rsc.li/greenchem

Covalent organic frameworks (COFs) have emerged as highly promising photocatalysts for hydrogen peroxide ($H_2O_2$) production due to their flexible structural designability and π–π conjugated backbone. However, the limited efficiency of electron–hole pair separation during COF photocatalysis remains a major challenge. Herein, a donor–acceptor (D–A) type COF containing a triazine functional group, namely TPB–TPT-COF, was concisely designed and synthesized for $H_2O_2$ production *via* photocatalysis. Owing to its enhanced carrier separation and transport, TPB–TPT-COF exhibited a remarkable $H_2O_2$ production rate of 6740 μmol $g^{-1}$ $h^{-1}$ from pure water and oxygen without any sacrificial agent under visible light irradiation, which is three times higher compared to its isomeric TPB-COF. Further experimental and theoretical investigations revealed that the photocatalytic processes of TPB–TPT-COF proceed *via* dominant $2e^-$ oxygen reduction reaction (ORR) pathways ($O_2 \rightarrow {}^{\bullet}O_2^- \rightarrow H_2O_2$ and $O_2 \rightarrow {}^{\bullet}O_2^- \rightarrow {}^1O_2 \rightarrow H_2O_2$) and $4e^-$ water oxidation reaction (WOR) pathways. This study not only elucidates the impact of the D–A structure on the activity within photocatalytic reactions but also provides novel design strategies for the improvement of photocatalytic $H_2O_2$ production.

## Green foundation

1. In this research, the photocatalytic approach is used to produce hydrogen peroxide from water and oxygen, replacing the traditional palladium-catalyzed method. This method uses solar energy and renewable resources, reduces waste, and eliminates the pollution caused by metal catalysts.
2. A donor–acceptor (D–A) COF (TPB–TPT-COF) was concisely synthesized for $H_2O_2$ production *via* photocatalysis. The enhanced carrier separation and transport of TPB–TPT-COF enabled it to exhibit a remarkable $H_2O_2$ production rate without any sacrificial agent. It outperforms most reported COF photocatalysts for $H_2O_2$ synthesis, relying solely on a triazine functional core to construct the D–A system.
3. Future work will optimize COF photocatalysts for $H_2O_2$ production, scale up experiments for industrial applications, and integrate them with organic oxidation processes for the green synthesis of high-value chemicals.

## 1. Introduction

Hydrogen peroxide ($H_2O_2$) is an important industrial chemical and an environmentally friendly oxidant, with extensive applications in environmental purification, chemical synthesis, and medical disinfection.[1] However, the traditional method of $H_2O_2$ production using palladium catalysts generates by-products, leading to environmental pollution.[2] In contrast, the photocatalytic process that utilizes readily available oxygen and water as natural substrates exhibits significant potential for $H_2O_2$ synthesis.[3,4] Early photocatalysts were mainly based on inorganic semiconductors, like $TiO_2$,[5,6] $BiVO_4$,[7,8] *etc*. Their limited tunability of chemical structures and electronic absorption properties restrict visible-light utilization, thereby hindering breakthroughs in photocatalytic $H_2O_2$ production.[9,10]

---

[a] *Key Laboratory of Eco-functional Polymer Materials of the Ministry of Education, Key Laboratory of Polymer Materials of Gansu Province, College of Chemistry and Chemical Engineering, Northwest Normal University, Lanzhou 730070, China. E-mail: lilihua202109@163.com, magf@nwnu.edu.cn*
[b] *School of Chemistry & Chemical Engineering, Linyi University, Linyi, 276000, China*
[c] *Heilongjiang Provincial Key Laboratory of $CO_2$ Resource Utilization and Energy Catalytic Materials, School of Material Science and Chemical Engineering, Harbin University of Science and Technology, Harbin 150040, PR China*
[d] *Key Laboratory of Low-Dimensional Quantum Structures and Quantum Control of Ministry of Education, Institute of Interdisciplinary Studies, Key Laboratory for Multifunctional Ionic Electronic Materials and Devices of Hunan Normal University, Changsha 410081, China. E-mail: hpzhou@hunnu.edu.cn*
[e] *State Key Laboratory of Low Carbon Catalysis and Carbon Dioxide Utilization, Lanzhou Institute of Chemical Physics, Chinese Academy of Sciences, Lanzhou 730000, Gansu, China*

† Electronic supplementary information (ESI) available. See DOI: **https://doi.org/10.1039/d5gc01754h**

‡ These authors contributed to this work equally.

Recently, covalent organic frameworks (COFs),[11] as porous crystalline organic polymers, have emerged in the field of photocatalytic synthesis of $H_2O_2$ due to their unique structural advantages. Their highly crystalline structure and ordered pore architecture shorten the migration pathways of photogenerated carriers and accelerate the diffusion of substrate molecules.[12] Their π–π conjugated structure reduces the charge recombination probability, extending the carrier lifetime.[13] COF frameworks can be directionally tuned to enhance their light-absorbing properties by introducing various functional groups such as sulfone,[14] porphyrin,[15] hydroxyl,[16] cyano,[17] benzothiazole,[18] heptazine,[19] pyrene,[20] thiophene,[21] acetylene,[22] *etc*. In 2020, Van Der Voort first applied a COF containing (diarylamino) benzene for photocatalytic $H_2O_2$ production, achieving a $H_2O_2$ generation rate of 234 μmol $g^{-1}$ $h^{-1}$.[23] Through functional group modification and structural regulation, COFs have made remarkable progress in improving $H_2O_2$ production. However, optimizing the efficiency of COF photocatalysts for industrial applications still faces key challenges. These include rapid electron–hole recombination, efficient reactant adsorption–desorption capacity, and long-term stability of catalysts in high-concentration $H_2O_2$, *etc*.[24–26]

The construction of donor–acceptor (D–A) structures could enhance the separation of photogenerated carriers due to the intrinsic electronic push–pull effect between donor and acceptor groups.[27–29] For example, Chen's group synthesized an *s*-heptazine-based COF with spatially separated redox centers, achieving a photocatalytic yield of 1750 μmol $g^{-1}$ $h^{-1}$ without any sacrificial agent.[30] Xue designed a methoxy functionalized D–A COF with (diarylamino)benzene as the donor and thiazolo [5,4-*d*]thiazole as the acceptor, and realized a $H_2O_2$ yield of 3238 μmol $g^{-1}$ $h^{-1}$.[31] Jiang's group incorporated triphenylene and diphenylbutadiyne into a hydrophilic D–A COF, enabling efficient hole and electron transport and achieving a production rate of 7200 μmol $g^{-1}$ $h^{-1}$.[32] This rational design provides a new idea for the optimization of photocatalytic performance, but most existing D–A systems are complex with low $H_2O_2$ production, which restrict their use in industrial processes. Therefore, designing more accessible D–A structure COFs to achieve bulk production of $H_2O_2$ becomes a future development direction.

On this basis, the D–A TPB–TPT-COF was concisely designed and synthesized for photocatalytic $H_2O_2$ production. This was constructed by introducing triazine functional groups into 4,4′,4″-(1,3,5-triazine-2,4,6-triyl)trianiline (TPT-$NH_2$) as the electron acceptor and 1,3,5-tris(4-formylphenyl)benzene (TPB-CHO) as the donor *via* the Schiff base condensation reaction (Fig. 1). The D–A structure endows TPB–TPT-COF with highly efficient charge separation capability, which results in a photocatalytic $H_2O_2$ generation rate of up to 6740 μmol $g^{-1}$ $h^{-1}$ from pure water and oxygen under visible light irradiation (λ > 420 nm), which is more than three times higher than that of TPB-COF without the triazine unit (2030 μmol $g^{-1}$ $h^{-1}$). Experimental and theoretical investigations confirmed that the photocatalytic process involves a combination of the $2e^-$ oxygen reduction reaction (ORR) and the $4e^-$ water oxidation reaction (WOR).

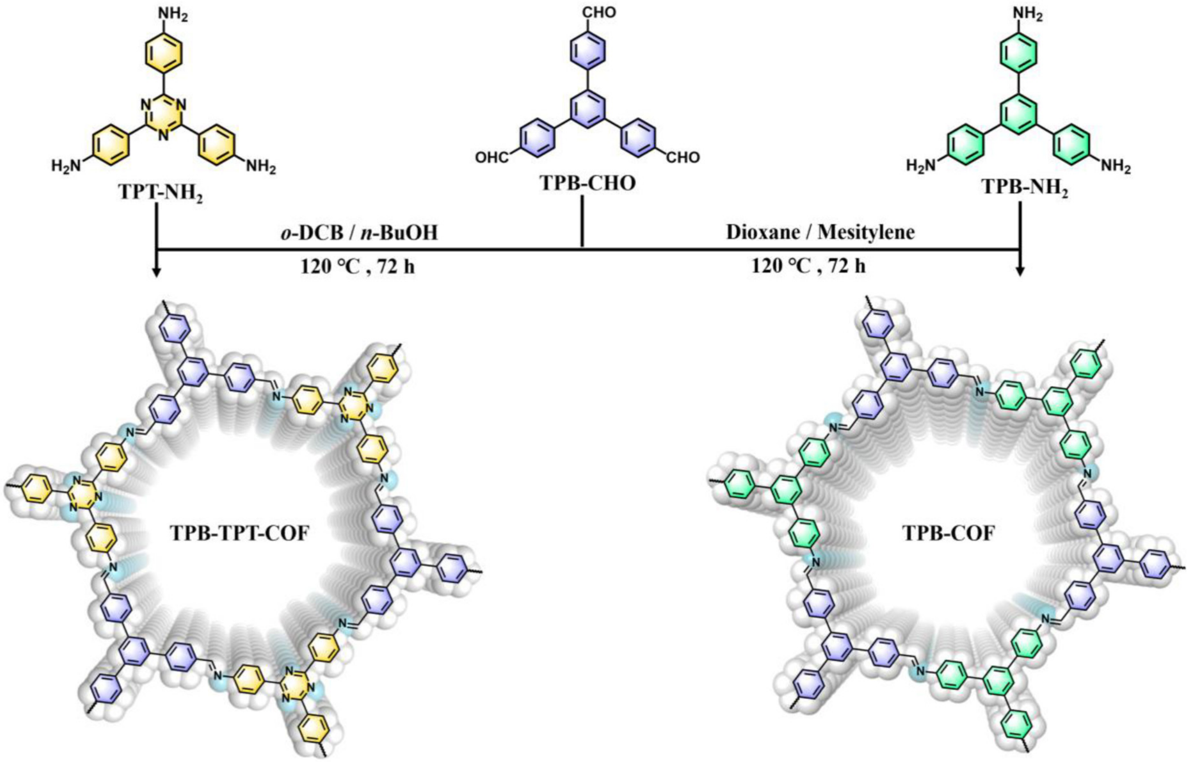

**Fig. 1** Schematic synthesis of TPB–TPT-COF and TPB-COF.

## 2. Results and discussion

### 2.1. Synthesis and characterisation of catalysts

Two target COFs, namely TPB–TPT-COF and TPB-COF, were synthesized using two amine monomers (TPT-$NH_2$ and TPB-$NH_2$) and 1,3,5-tris(4-formylphenyl)benzene (TPB-CHO), respectively, through a solvent-thermal condensation reaction at 120 °C *via* modified reported methods (Fig. 1).[33] Firstly, the crystallinity of the two COFs was characterized by powder X-ray diffraction (PXRD). The PXRD pattern of TPB–TPT-COF shows a distinct peak at an angle of $2\theta = 4.1°$, corresponding to the (100) plane. In addition, three relatively weak peaks can be observed for TPB–TPT-COF at angles of 7.1°, 8.1°, and 10.8°, which can be attributed to the presence of the (110), (200), and (210) planes. Meanwhile, the PXRD pattern of TPB-COF exhibits a high degree of similarity to that of TPB–TPT-COF. The structural models of the two COFs were simulated as shown in Fig. 2a and b, and they are in good agreement with the experimental PXRD data when considering the AA stacking mode (Fig. 2c, d and Table S1†). The chemical structures of TPB–TPT-COF and TPB-COF were characterized by Fourier transform infrared (FT-IR) spectroscopy and solid-state $^{13}C$ nuclear magnetic resonance ($^{13}C$-ssNMR) spectroscopy. The FT-IR analysis shows decreased intensities for N–H and C=O groups in both COFs, along with new peaks at approximately 1620 $cm^{-1}$, confirming the successful formation of imine bonds (Fig. S1†).[34] Furthermore, $^{13}C$-ssNMR spectra exhibit characteristic peaks around 157 ppm (Fig. S2†), indicating the presence of carbon signals associated with the imine bond in both COFs. The composition and chemical states of the elements in TPB–TPT-COF and TPB-COF were determined using X-ray photoelectron spectroscopy (XPS) (Fig. S3†). The porosity of these COFs was further determined using $N_2$ adsorption–desorption isotherms at 77 K (Fig. 2e and f). The Brunauer–Emmett–Teller (BET) analysis shows that the calculated specific surface area values of TPB–TPT-COF and TPB-COF are 684 and 307 $m^2$ $g^{-1}$, (Fig. S4†), respectively. The average pore sizes for the two COFs are 1.2–2.0 nm. Thermogravimetric analysis (TGA) curves show that TPB–TPT-COF and TPB-COF have excellent thermal-stability at temperatures up to 527 °C (Fig. S5†). The morphologies and microstructures of the COFs were investigated using scanning electron microscopy (SEM) and transmission electron microscopy (TEM). Fig. S6† shows that TPB–TPT-COF exhibits an irregular nanoparticle stacking morphology and TPB-COF has an irregular pie-like structure. Contact angle measurements reveal that TPB–TPT-COF is superhydrophilic (21.3°), while TPB-COF is hydrophobic (140.8°) (Fig. S7†).

### 2.2. Photocatalytic $H_2O_2$ production performance

After characterizing the porous crystalline structures of TPB–TPT-COF and TPB-COF, their photoelectronic properties were investigated. UV-visible diffuse reflectance spectra exhibited broad visible light absorption for both COFs, confirming their

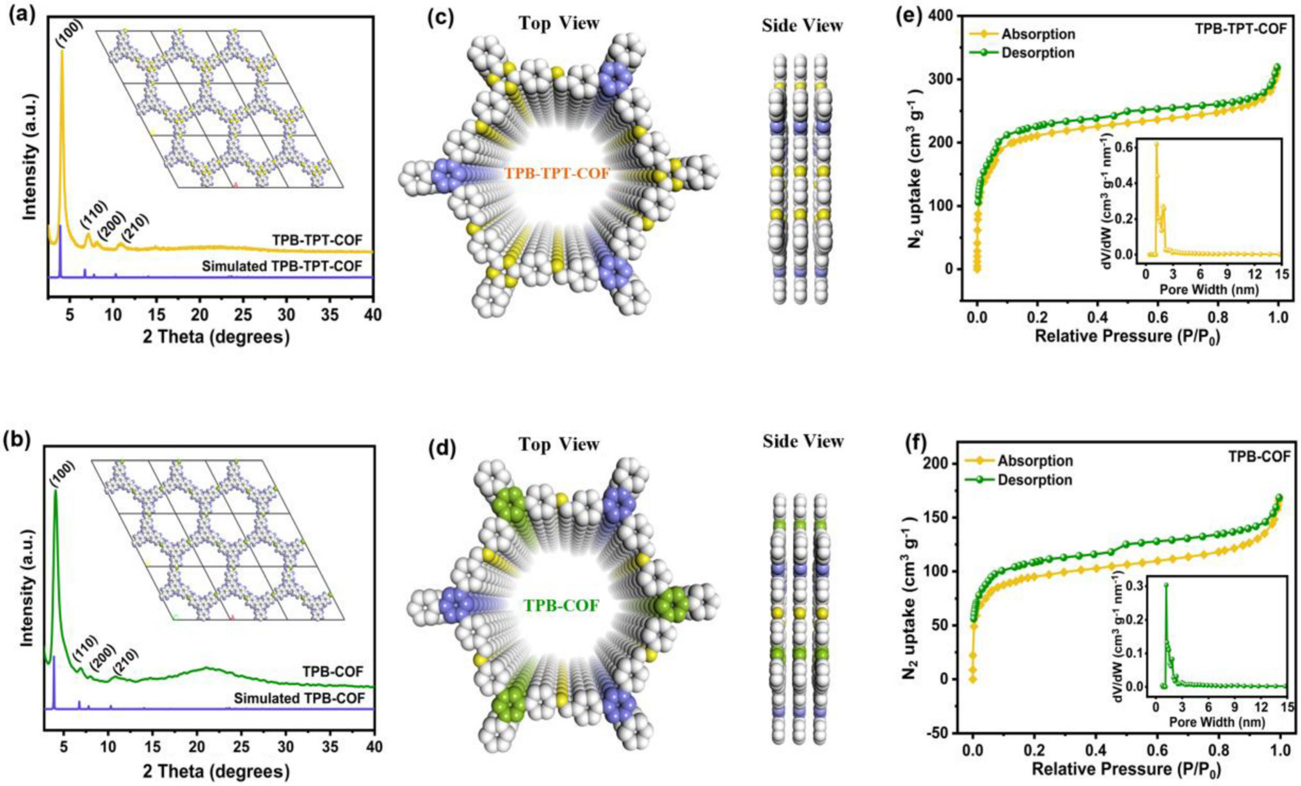

**Fig. 2** (a and b) Experimental and simulated PXRD plots of TPB–TPT-COF and TPB-COF. (c and d) Top and side views of the eclipsed AA-stacking models. (e and f) $N_2$ isotherms and pore size distributions of both COFs.

excellent visible light harvesting. The Tauc plot determined the optical band gaps of 2.67 eV and 2.65 eV for TPB–TPT-COF and TPB-COF, respectively (Fig. 3a). Mott–Schottky curves revealed n-type semiconductor characteristics with flat band potentials measured at −0.80 V and −0.89 V, respectively (relative to Ag/AgCl at pH = 7) (Fig. S8†). The energy band diagrams in Fig. 3b show that the conduction band ($C_B$) potentials are −0.60 V and −0.69 V (relative to NHE) and the valence band ($V_B$) potentials are +2.07 V and +1.96 V, respectively.[35,36] Thermodynamically, since both $C_B$ potentials are more negative than the potential required for $O_2$ generation from superoxide ions (−0.33 V *vs.* NHE at pH = 7), this indicates that TPB–TPT-COF and TPB-COF are promising candidates for the ORR.[37]

The separation and migration of photogenerated electrons and holes were further investigated. Fig. 3c shows fluorescence decay curves of TPB–TPT-COF and TPB-COF, with lifetimes of 1.37 ns and 0.23 ns, respectively. In the photoluminescence spectra, TPB–TPT-COF exhibits lower fluorescence response than TPB-COF (Fig. S9†). These results indicate that the inhibitory effect of TPB–TPT-COF on photoexcited carrier recombination is better than that of TPB-COF. Electrochemical impedance spectroscopy (EIS) reveals faster charge transport in TPB–TPT-COF due to its smaller semicircle radius (Fig. 3d). Additionally, TPB–TPT-COF exhibits higher photocurrent response intensity than TPB-COF (Fig. 3e), suggesting more photogenerated electrons for photocatalysis. Density functional theory (DFT) calculations show that triazine fragments of TPB–TPT-COF have significant negative potential energy, enhancing charge transfer and separation efficiency (Fig. 3f). All results demonstrate that the incorporation of a D–A structure into TPB–TPT-COF improves carrier separation and transport.

We next assessed the photocatalytic $H_2O_2$ production performance of these COFs under visible light irradiation ($\lambda$ >

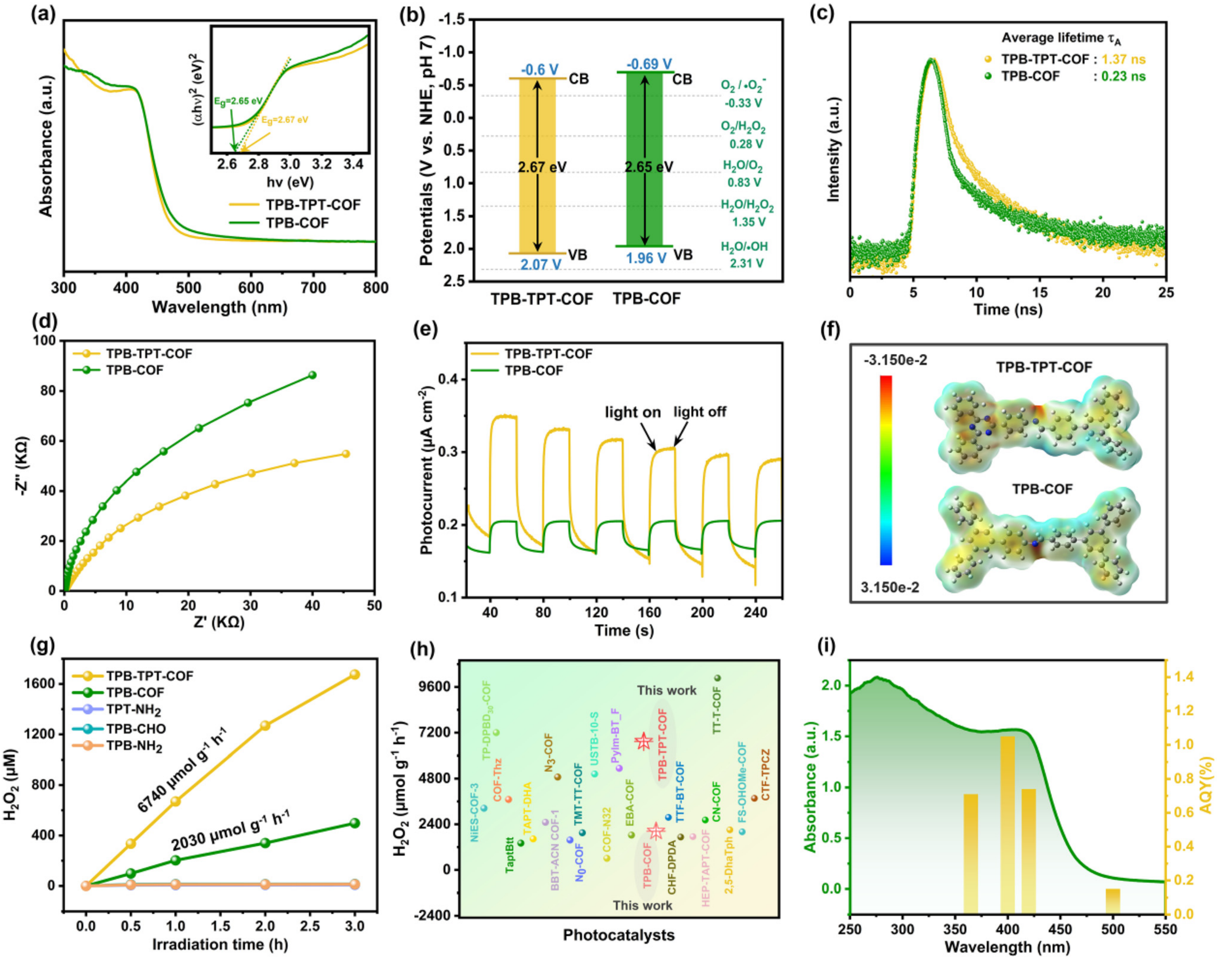

**Fig. 3** (a) UV-visible diffuse reflectance spectra and Tauc plots of TPB–TPT-COF and TPB-COF. (b) Energy band structure maps. (c) Fluorescence decay curves. (d) EIS plots. (e) Photocurrent response curves. (f) Electrostatic potential-mapped molecular van der Waals surface. (g) Photocatalytic performance *versus* time curves for TPB–TPT-COF, TPB-COF and monomers. (h) Comparison of $H_2O_2$ production rates of both COFs with other reported D–A photocatalysts. (i) AQYs at different wavelengths.

420 nm). The concentration of $H_2O_2$ was determined by iodometric analysis (Fig. S10†).[38] The dosage of TPB–TPT-COF was optimized, as shown in Fig. S11.† In $H_2O_2$ photodecomposition experiments, the two COFs caused negligible $H_2O_2$ decomposition (Fig. S12†). TPB–TPT-COF and TPB-COF were continuously reacted in oxygen and pure water for 3 hours without the addition of any sacrificial agent. As shown in Fig. 3g, both COF monomers produced negligible $H_2O_2$, indicating that the construction of a π-conjugated COF framework is crucial for efficient photocatalysis. TPB–TPT-COF has a significantly higher rate of $H_2O_2$ production (6740 μmol $g^{-1}$ $h^{-1}$) compared to TPB-COF (2030 μmol $g^{-1}$ $h^{-1}$). This enhanced performance can be attributed to the D–A structure inherent in TPB–TPT-COF, which facilitates an increased carrier separation and transport, thereby improving the photocatalytic efficiency. In addition, the superhydrophilic property (with a contact angle of 21.3°) exhibited by the aforementioned TPB–TPT-COF significantly enhances the affinity of the material for water molecules, thereby accelerating the transport process of the reaction substrates. This property is also one of the key factors for improving the photocatalytic efficiency.[39] The catalytic performance of TPB–TPT-COF surpasses those of most reported D–A photocatalysts for $H_2O_2$ synthesis, despite relying solely on the incorporation of a triazine functional core to construct the D–A system (Fig. 3h and Table S2†). The apparent quantum yield (AQY) of TPB–TPT-COF under monochromatic light irradiation at different incident wavelengths shows a strong correlation with its absorption spectra, peaking at 1.05% at 400 nm (Fig. 3i). The apparent quantum yield (AQY) of PTB-TPT-COF is relatively low, which may be attributed to its insufficient visible light absorption (<600 nm), and the lattice defects in the powder-crystalline structure of the catalyst leading to the facile loss of carriers.[40] The solar energy conversion to chemical energy (SCC) is determined to be 0.14%, exceeding the average photosynthetic efficiency of plants (0.10%).[41] TPB–TPT-COF exhibited excellent photocatalytic stability during the initial four cycles (Fig. S13†). However, its performance dropped significantly in the fifth cycle due to its reduced crystallinity and chemical structure degradation, as confirmed by its PXRD and FT-IR spectra (Fig. S14 and S15†).[42] For practical applications, long-term catalytic reaction parameters are very important metrics.[43] TPB–TPT-COF demonstrated photocatalytic activity and durability for up to 48 hours in pure water (Fig. S16†).

### 2.3. Reaction mechanism studies

A series of controlled experiments was carried out to elucidate the pathway of photocatalytic $H_2O_2$ production. Both COFs showed negligible $H_2O_2$ yields in the absence of light. Under both air and $N_2$ atmospheres, the yield of $H_2O_2$ decreases as the oxygen concentration diminishes, suggesting that the ORR plays an indispensable role in the reaction process. When $AgNO_3$ ($e^-$ sacrificial agent) was added to the system, the production of $H_2O_2$ was significantly reduced, indicating that the ORR pathway plays a dominant role in photocatalytic $H_2O_2$ generation (Fig. 4a).

Firstly, a systematic study was conducted on the ORR pathways involved in the $H_2O_2$ photocatalytic process of TPB–TPT-COF and TPT-COF, utilizing scavengers to investigate the role of reactive oxygen species in the ORR pathway. Adding *p*-benzoquinone (*p*-BQ, for $^{\bullet}O_2^-$) and β-carotene (for $^1O_2$) scavengers significantly decreased the $H_2O_2$ generation rate after 1 h of irradiation (Fig. 4b); this indicates that $^{\bullet}O_2^-$ and $^1O_2$ are the key active species in the ORR process. Electron paramagnetic resonance (EPR) experiments further characterized reactive oxygen species using 5,5-dimethyl-1-pyrroline *N*-oxide (DMPO) and 2,2,6,6-tetramethylpiperidine (TEMP) scavengers. After 5 min of visible light exposure, distinct EPR signals were observed for $^{\bullet}O_2^-$ and $^1O_2$ (Fig. 4c and d). Under identical conditions, TPB–TPT-COF showed significantly higher EPR signal intensities than TPB-COF, confirming its superior efficiency in generating $^{\bullet}O_2^-$ and $^1O_2$. Adding *p*-BQ into $^1O_2$-TEMP systems reduced the $^1O_2$ signal intensity in both COFs (Fig. 4d), suggesting $^1O_2$ formation *via* charge transfer between $^{\bullet}O_2^-$ radicals and holes.[44]

The concentrations of $^{\bullet}O_2^-$ and $^1O_2$ were re-evaluated using the colorimetric method with nitroblue tetrazolium chloride (NBT) for $^{\bullet}O_2^-$ detection and 1,3-diphenylisobenzofuran (DPBF) for $^1O_2$ quantification. As shown in Fig. 4e, f and S17 and 18,† TPB–TPT-COF exhibited higher production levels of $^{\bullet}O_2^-$ and $^1O_2$ compared to TPB-COF. Furthermore, upon the addition of *p*-BQ to the DPBF solution, the concentration of $^1O_2$ decreased in both TPB–TPT-COF and TPB-COF systems; this also indicates $^1O_2$ formation *via* charge transfer between $^{\bullet}O_2^-$ radicals (Fig. 4f and S18†). Combining the results of the EPR signals and UV/Vis absorption spectra, we completely confirmed that both TPB–TPT-COF and TPB-COF were able to generate $^{\bullet}O_2^-$ and partly convert it to $^1O_2$. The rotating disc electrode (RDE) technique was used to investigate the electron transfer numbers in the ORR (Fig. S19†). TPB–TPT-COF has an average transfer number of nearly 2, which is higher compared to TPB-COF, indicating that TPB–TPT-COF has a higher selectivity towards $H_2O_2$ production (Fig. 4g). These pieces of evidence reveal two indirect pathways in the photogenerated two-electron oxygen reduction reactions of TPB–TPT-COF and TPB-COF: $O_2 + e^- \rightarrow {}^{\bullet}O_2^-$, ${}^{\bullet}O_2^- + 2H^+ + e^- \rightarrow H_2O_2$ and $O_2 + e^- \rightarrow {}^{\bullet}O_2^-$, ${}^{\bullet}O_2^- + h^+ \rightarrow {}^1O_2$, ${}^1O_2 + 2H^+ + 2e^- \rightarrow H_2O_2$.[45]

To explore the WOR process involved in the photocatalytic system, the water oxidation half-reaction of TPB–TPT-COF and TPB-COF was studied. After the addition of *t*-butyl alcohol (TBA), the $H_2O_2$ yield remained almost unchanged, thereby excluding the involvement of $^{\bullet}OH$ in $H_2O_2$ formation. When $AgNO_3$ was added and Ar flowed continuously, no $H_2O_2$ was detected (Fig. 4a), ruling out its formation *via* the $2e^-$ WOR.[41] Oxygen was produced from TPB–TPT-COF in an argon-saturated aqueous solution using $AgNO_3$ as the sacrificial electron acceptor (Fig. 4h). This suggests that TPB–TPT-COF primarily facilitates the conversion of water to oxygen *via* the $4e^-$ WOR reaction pathway.[46] Subsequently, an isotope labeling experiment with $^{18}O_2$ was conducted. Following photocatalytic irradiation of the $H_2{}^{18}O$-COFs suspension, the presence of $^{18}O_2$ (*m*/*z* = 36) in both COFs was detected, providing further

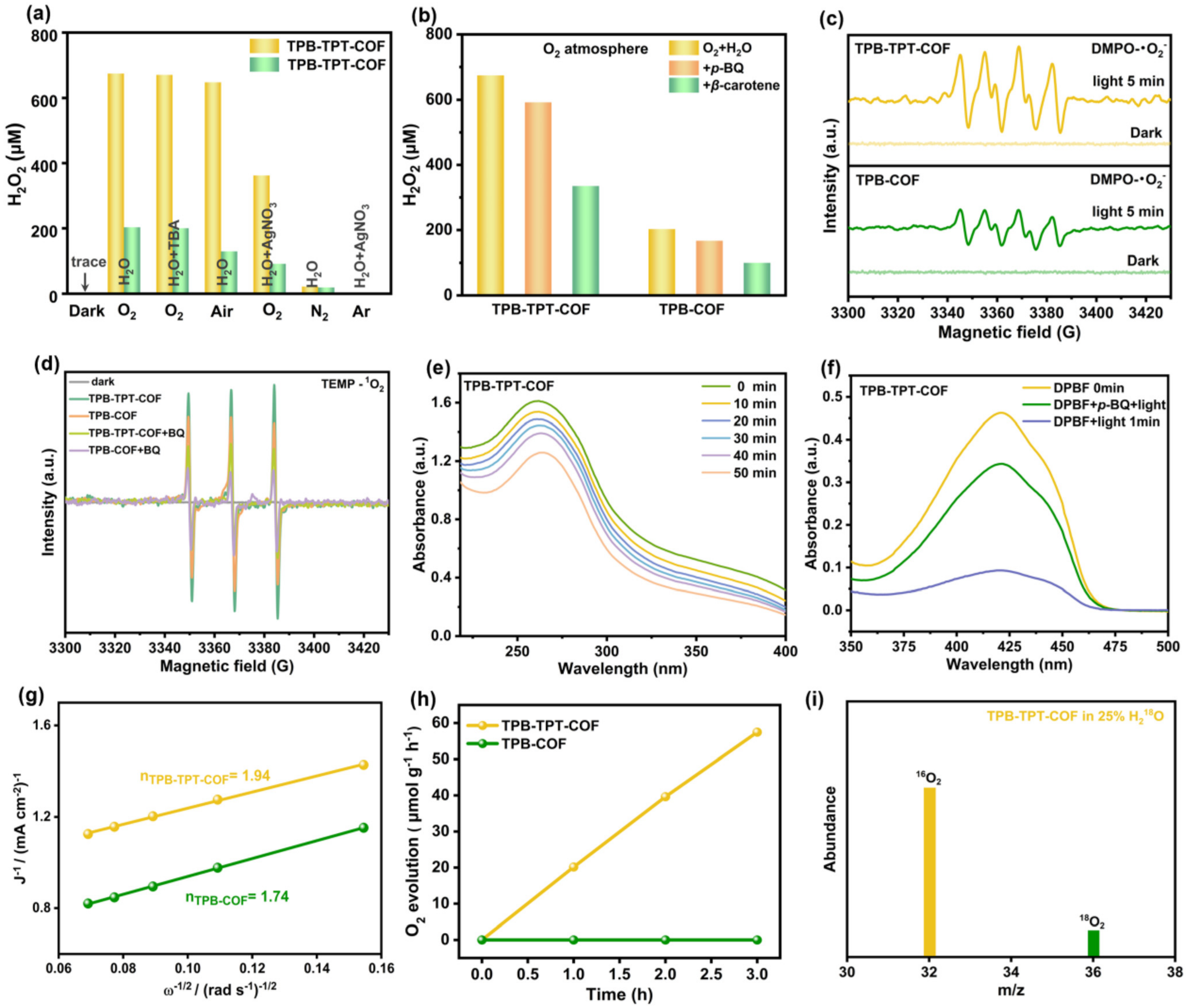

**Fig. 4** (a) $H_2O_2$ production rates of both COFs under different conditions. (b) $H_2O_2$ yield of the COFs after 1 h of light exposure under an $O_2$ atmosphere in the presence of *p*-BQ (1 mM) and β-carotene (1 mM). (c) EPR signals for $^{\bullet}O_2^-$ generation. (d) EPR signals for $^1O_2$ generation. (e) Detection of $^{\bullet}O_2^-$ of TPB–TPT-COF using NBT. (f) Detection of $^1O_2$ of TPB–TPT-COF using DPBF. (g) Average electron transfer numbers obtained by RDE calculations. (h) Photocatalytic $O_2$ evolution for the two COFs. (i) $H_2{}^{18}O$ isotope labelling experiment for TPB–TPT-COF.

confirmation of the $4e^-$ WOR pathway (Fig. 4i and S20†).[47] Therefore, it is proposed that the $2e^-$ ORR and the $4e^-$ WOR are the predominant reaction pathways for the photo-generated $H_2O_2$ in TPB–TPT-COF and TPB-COF.

## 2.4. Theoretical analysis

The intermediate species during the photocatalytic process of TPB–TPT-COF and TPB-COF (Fig. S21†) were further monitored by *in situ* diffuse reflectance infrared Fourier transform spectroscopy (DRIFTS). As shown in Fig. 5a, after irradiation, the peaks of TPB–TPT-COF at 1194–1132 $cm^{-1}$ and 1252 $cm^{-1}$ were gradually increased, attributed to the intermediates $^{\bullet}O_2^-$ and superoxide *O–OH. The peaks at 965 $cm^{-1}$ correspond to the O–O bond stretching vibrations. The presence of C═C–O (1344 $cm^{-1}$) and C–O–O (1004 $cm^{-1}$) suggests $O_2$ adsorption onto aromatic carbons. Vibrational peaks at 1089 $cm^{-1}$ (C–OH) and 1428/1399 $cm^{-1}$ (C–O) can be attributed to intermediate species involved in water oxidation.[48] The $^{\bullet}O_2^-$ intermediate peak of TPB-COF was much weaker than that of TPB–TPT-COF, which may also explain the low yield of TPB-COF (Fig. S21†).

DFT calculations were further performed to investigate the reaction mechanism. The optimized periodic structures of TPB–TPT-COF and TPB-COF are shown in Fig. S22.† $O_2$ and $H_2O$ are adsorbed at the potential active sites of TPB–TPT-COF and TPB-COF (Fig. S23 and S24†).[49] Then, the Gibbs free energy ($\Delta G$) during the $2e^-$ ORR and $4e^-$ WOR processes was calculated. In the indirect $2e^-$ ORR process, the formation of $H_2O_2$ involves several key intermediates, including $*O_2$, *OOH,

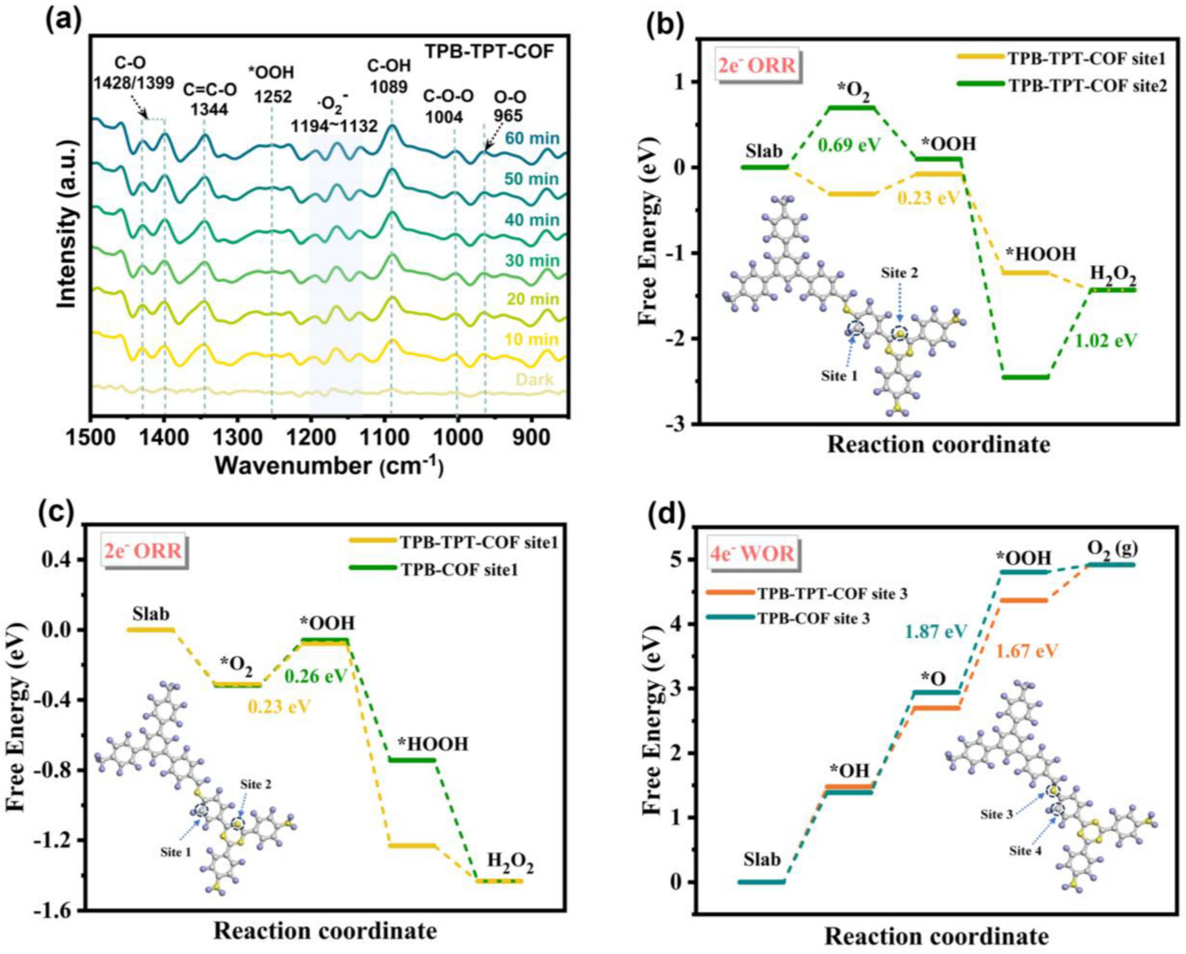

**Fig. 5** (a) *In situ* DRIFT spectra of TPB–TPT-COF recorded during photocatalytic $H_2O_2$ evolution. (b) Calculated Δ*G* diagrams of the oxygen reduction reaction on different active sites for TPB–TPT-COF. (c) Δ*G* of TPB–TPT-COF and TPB-COF for the ORR at site 1. (d) Δ*G* of TPB–TPT-COF and TPB-COF for the WOR at site 3.

*HOOH, and HOOH. Site 2 of TPB–TPT-COF exhibits a relatively high energy barrier of 0.69 eV in the rate-limiting step of the conversion of $O_2$ to $*O_2$ (Fig. 5b), which impedes the timely conversion of $O_2$ adsorbed at the active sites into $*O_2$. In the subsequent conversion step from $*O_2$ to the critical intermediate *OOH, the free energy change at site 1 of TPB–TPT-COF is more gradual, with a significantly lower energy barrier than that of site 2. Additionally, site 2 has a high Δ*G* of 1.02 eV for the decomposition of *HOOH, which is unfavorable for the generation of $H_2O_2$.[50,51] Based on the above adsorption sites and Δ*G* calculations, it was found that site 1 on the phenyl ring near the imine bond in TPB–TPT-COF is the active region for the two-step $2e^-$ ORR, and site 3 of the imine bond is the active position for the $4e^-$ WOR (Fig. S25†). The potential active sites of TPB-COF are shown in Fig. S25 and 26.† In addition, the free energy distribution diagrams of the two COFs at site 1 and site 3 were directly compared (see Fig. 5c and d). It was observed that, in the rate-determining step (RDS) associated with the formation of the intermediate *OOH, the energy barrier for TPT–TPB-COF (0.23 eV) was lower than that of TPB-COF (0.26 eV). And the Δ*G* value for the $4e^-$ WOR pathway indicates the rate-determining step energy barrier at site 3 in TPB–TPT-COF (1.67 eV) is lower than that in TPB-COF (1.87 eV). These results indicate that the catalytic activity of TPT–TPB-COF is superior to that of TPB-COF.

## 3. Conclusion

In summary, the TPB–TPT-COF photocatalyst with a D–A structure was successfully synthesized by incorporating triazine units; it achieved an impressive production rate of 6740 μmol $g^{-1}$ $h^{-1}$ for $H_2O_2$ from pure water and $O_2$ without any sacrificial agent. Photoelectronic characterization confirmed that the D–A structure in TPB–TPT-COF enhances the separation and transport of carriers, thereby significantly improving its photocatalytic performance. Experimental investigations and DFT calculations elucidated the intermediate species, potential reaction sites and plausible reaction pathways. These findings provide a feasible strategy for the design and development of efficient photocatalysts for $H_2O_2$ production.

## Author contributions

Lihua Li: conceptualization, resources, funding acquisition, and writing – review & editing. Xin Yao: formal analysis, writing – original draft, investigation, methodology, and software. Weizhi Ou: investigation, software, and methodology. Jing Chai: validation and investigation. Ru Ma and Chenglong Ran: fluorescence emission, solid-state UV-vis absorption, and elemental analysis experiments. Anzhi Ma and Xiaojun Shi: electrochemistry measurements. Pifeng Wei: supervision and resources. Hong Dong: supervision and writing – review & editing. Hongpeng Zhou: theoretical calculation. Wenbing Yang: GC-MS. Hai-Chao Hu: isotope labelling. Jian-Feng Wu: supervision and resources. Hui Peng: supervision and resources. Guofu Ma: resources, funding acquisition, and supervision.

## Conflicts of interest

The authors declare no conflict of interest.

## Data availability

All data supporting this study are included in the article and its ESI.†

## Acknowledgements

We thank Prof. Yong Ding (Lanzhou University) and Dr Qin Zhou (Dalian Institute of Chemical Physics, Chinese Academy of Sciences) for helping with the photocatalytic oxygen production. This work was supported by the National Natural Science Foundation of China (22401235; 22472181; 22409060 and U22A2078), the enterprise project of China Northern Rare Earth (Group) High-Tech Co., Ltd (BFXT-2023-D-0048) and Hunan Provincial Natural Science Foundation of China (025JJ60074).

## References

1 R. Hage and A. Lienke, *Angew. Chem., Int. Ed.*, 2005, **45**, 206–222.
2 J. M. Campos-Martin, G. Blanco-Brieva and J. L. G. Fierro, *Angew. Chem., Int. Ed.*, 2006, **45**, 6962–6984.
3 H. Hou, X. Zeng and X. Zhang, *Angew. Chem., Int. Ed.*, 2020, **59**, 17356–17376.
4 X. Zeng, Y. Liu, X. Hu and X. Zhang, *Green Chem.*, 2021, **23**, 1466–1494.
5 B. He, Z. Wang, P. Xiao, T. Chen, J. Yu and L. Zhang, *Adv. Mater.*, 2022, **34**, 2203225.
6 Y. Shiraishi, S. Kanazawa, D. Tsukamoto, A. Shiro, Y. Sugano and T. Hirai, *ACS Catal.*, 2013, **3**, 2222–2227.
7 H. L. Tan, C. H. T. Chai, J. Z. X. Heng, Q. V. Thi, X. Wu, Y. H. Ng and E. Ye, *Adv. Sci.*, 2024, **12**, 2407801.
8 S. Shi, Y. Song, Y. Jiao, D. Jin, Z. Li, H. Xie, L. Gao, L. Sun and J. Hou, *Nano Lett.*, 2024, **24**, 6051–6060.
9 Z. Yong and T. Ma, *Angew. Chem., Int. Ed.*, 2023, **62**, e202308980.
10 J. Hao, Y. Tang, J. Qu, Y. Cai, X. Yang and J. Hu, *Small*, 2024, **20**, 2404139.
11 A. P. Côté, A. I. Benin, N. W. Ockwig, M. O'Keeffe, A. J. Matzger and O. M. Yaghi, *Science*, 2005, **310**, 1166–1170.
12 H. Wang, X. Liu, P. Niu, S. Wang, J. Shi and L. Li, *Matter*, 2020, **2**, 1377–1413.
13 P. H. de Oliveira Neto, D. A da Silva Filho, W. F. da Cunha, P. H. Acioli and G. M. e Silva, *J. Phys. Chem. C*, 2015, **119**, 19654–19659.
14 C. Shu, X. Yang, L. Liu, X. Hu, R. Sun, X. Yang, A. I. Cooper, B. Tan and X. Wang, *Angew. Chem., Int. Ed.*, 2024, **63**, e202403926.
15 A. Yoshikawa, H. Shigemitsu, X. Li, M. Fujitsuka, Y. Osakada and T. Kida, *ACS Appl. Energy Mater.*, 2024, **7**, 9084–9088.
16 D. Cao, J. Du, J. Li, Q. Sun, J. Guan and J. Liu, *ACS Catal.*, 2025, **15**, 3584–3594.
17 Z. Yu, F. Yu, M. Xu, S. Feng, J. Qiu and J. Hua, *Adv. Sci.*, 2025, **12**, 2415194.
18 L. Wang, J. Sun, M. Deng, C. Liu, S. Ataberk Cayan, K. Molkens, P. Geiregat, R. Morent, N. De Geyter, J. Chakraborty and P. Van Der Voort, *Catal. Sci. Technol.*, 2023, **13**, 6463–6471.
19 C. Wang, T. Y. Qiu, Y. N. Zhao, Z. L. Lang, Y. G. Li, Z. M. Su and H. Q. Tan, *Adv. Energy Mater.*, 2023, **13**, 2301634.
20 J. Sun, H. Sekhar Jena, C. Krishnaraj, K. Singh Rawat, S. Abednatanzi, J. Chakraborty, A. Laemont, W. Liu, H. Chen, Y. Y. Liu, K. Leus, H. Vrielinck, V. Van Speybroeck and P. Van Der Voort, *Angew. Chem., Int. Ed.*, 2023, **62**, e202216719.
21 H. Li, J. Shi, J. Deng, Z. Chen, Y. Li, W. Zhao, J. Wu, H. Wu, Y. Luo, D. Li and Q. Meng, *Adv. Mater.*, 2020, **32**, 1907396.
22 H. Yu, F. Zhang, Q. Chen, P. K. Zhou, W. Xing, S. Wang, G. Zhang, Y. Jiang and X. Chen, *Angew. Chem., Int. Ed.*, 2024, **63**, e202402297.
23 C. Krishnaraj, H. Sekhar Jena, L. Bourda, A. Laemont, P. Pachfule, J. Roeser, C. V. Chandran, S. Borgmans, S. M. J. Rogge, K. Leus, C. V. Stevens, J. A. Martens, V. Van Speybroeck, E. Breynaert, A. Thomas and P. Van Der Voort, *J. Am. Chem. Soc.*, 2020, **142**, 20107–20116.
24 S. Liu, M. Wang, Y. He, Q. Cheng, T. Qian and C. Yan, *Coord. Chem. Rev.*, 2023, **475**, 214882.
25 T. Hisatomi, J. Kubota and K. Domen, *Chem. Soc. Rev.*, 2014, **43**, 7520–7535.
26 R. Liu, Y. Chen, H. Yu, M. Položij, Y. Guo, T. C. Sum, T. Heine and D. Jiang, *Nat. Catal.*, 2024, **7**, 195–206.

27 S. Li, W. Wei, K. Chi, C. T. J. Ferguson, Y. Zhao and K. A. I. Zhang, *J. Am. Chem. Soc.*, 2024, **146**, 12386–12394.

28 L. Guo, L. Gong, Y. Yang, Z. Huang, X. Liu and F. Luo, *Angew. Chem., Int. Ed.*, 2024, **64**, e202414658.

29 K. Yu, L. Gong, Z. Huang, Z. Yu and F. Luo, *CCS Chem.*, 2024, DOI: **10.31635/ccschem.024.202405109**.

30 D. Chen, W. Chen, Y. Wu, L. Wang, X. Wu, H. Xu and L. Chen, *Angew. Chem., Int. Ed.*, 2023, **62**, e202217479.

31 D. M. Xue, Y. J. Zhang, J. W. Chen, H. Yang, R. J. Xie, S. C. Qi, Y. Q. Bu, F. Liu, H. H. Zhang and J. Lalevée, *Chem. Eng. J.*, 2024, **502**, 157874.

32 Y. Chen, R. Liu, Y. Guo, G. Wu, T. C. Sum, S. W. Yang and D. Jiang, *Nat. Synth.*, 2024, **3**, 998–1010.

33 J. Yang, A. Acharjya, M. Y. Ye, J. Rabeah, S. Li, Z. Kochovski, S. Youk, J. Roeser, J. Grüneberg, C. Penschke, M. Schwarze, T. Wang, Y. Lu, R. van de Krol, M. Oschatz, R. Schomäcker, P. Saalfrank and A. Thomas, *Angew. Chem., Int. Ed.*, 2021, **60**, 19797–19803.

34 J. Liu, C. Tuo, W. Y. Xiao, M. Y. Qi, Y. Yusran, Z. Wang, H. Li, C. Guo, J. Song, S. Qiu, Y. J. Xu and Q. Fang, *Angew. Chem., Int. Ed.*, 2025, **64**, e202416240.

35 Y. Nosaka and A. Y. Nosaka, *Chem. Rev.*, 2017, **117**, 11302–11336.

36 W. H. Koppenol, D. M. Stanbury and P. L. Bounds, *Free Radicals Biol. Med.*, 2010, **49**, 317–322.

37 X. Yang, Z. X. Pan, J. Y. Yue, X. Li, G. Liu, Q. Xu and G. Zeng, *Small*, 2024, **20**, 2405907.

38 L. Zhang, C. Wang, Q. Jiang, P. Lyu and Y. Xu, *J. Am. Chem. Soc.*, 2024, **146**, 29943–29954.

39 X. Bai, L. Guo, T. Jia and Z. Hu, *J. Mater. Chem. A*, 2024, **12**, 13116–13126.

40 X. Zhu, Y. Jia, Y. Liu, J. Xu, H. He, S. Wang, Y. Shao, Y. Zhai and Y. Zhu, *Angew. Chem., Int. Ed.*, 2024, **63**, e202405962.

41 Z. Zhang, Q. Zhang, Y. Hou, J. Li, S. Zhu, H. Xia, H. Yue and X. Liu, *Angew. Chem., Int. Ed.*, 2024, **63**, e202411546.

42 J. Y. Yue, L. P. Song, Y. F. Fan, Z. X. Pan, P. Yang, Y. Ma, Q. Xu and B. Tang, *Angew. Chem., Int. Ed.*, 2023, **62**, e202309624.

43 X. Wang, X. Yang, C. Zhao, Y. Pi, X. Li, Z. Jia, S. Zhou, J. Zhao, L. Wu and J. Liu, *Angew. Chem., Int. Ed.*, 2023, **62**, e202302829.

44 J. Y. Yue, J. X. Luo, Z. X. Pan, R. Z. Zhang, P. Yang, Q. Xu and B. Tang, *Angew. Chem., Int. Ed.*, 2024, **63**, e202405763.

45 J. Y. Yue, L. P. Song, Z. X. Pan, P. Yang, Y. Ma, Q. Xu and B. Tang, *ACS Catal.*, 2024, **14**, 4728–4737.

46 H. Xu, Y. Wang, Y. Xu, Q. Wang, M. Zhuang, Q. Liao and K. Xi, *Angew. Chem., Int. Ed.*, 2024, **63**, e202408802.

47 T. Yang, D. Zhang, A. Kong, Y. Zou, L. Yuan, C. Liu, S. Luo, G. Wei and C. Yu, *Angew. Chem., Int. Ed.*, 2024, **63**, e202404077.

48 W. Zhang, M. Sun, J. Cheng, X. Wu and H. Xu, *Adv. Mater.*, 2025, **37**, 2500913.

49 W. Wang, R. Zhang, H. Chu, Z. Zhan, Q. Huang, Z. Li, X. Wang, F. Bai and W. Zhou, *Small*, 2024, **21**, 2406527.

50 S. Feng, H. Cheng, F. Chen, X. Liu, Z. Wang, H. Xu and J. Hua, *ACS Catal.*, 2024, **14**, 7736–7745.

51 J. P. Liao, M. Zhang, P. Huang, L. Z. Dong, T. T. Ma, G. Z. Huang, Y. F. Liu, M. Lu, S. L. Li and Y. Q. Lan, *ACS Catal.*, 2024, **14**, 3778–3787.